



Cite this: *J. Mater. Chem. C*, 2018, 6, 9248

Luminescent MOF polymer mixed matrix membranes for humidity sensing in real status analysis†

Johannes M. Stangl,^a Dennis Dietrich,^b Alexander E. Sedykh,^a Christoph Janiak^b and Klaus Müller-Buschbaum^b *^a

Received 28th March 2018,
Accepted 30th July 2018

DOI: 10.1039/c8tc01454j

rsc.li/materials-c

Humidity sensing properties of luminescent metal–organic framework (MOF) polymer mixed-matrix membranes (MMMs) ${}^3_{\infty}[\text{Ba}_{0.98}\text{Eu}_{0.02}(\text{Im})_2]\text{@PSF}$ (Im = imidazolate, PSF = polysulfone Ultrason[®] S), ${}^3_{\infty}[\text{Sr}_{0.90}\text{Eu}_{0.10}(\text{Im})_2]\text{@PSF}$, and ${}^3_{\infty}[\text{Ce}(\text{Im})_3\text{ImH}]\text{-ImH@PSF}$ were investigated. MMMs show superior properties compared to bulk MOFs especially in stability, handling and long-term monitoring. In order to evaluate these films for such real status analyses, both their sensitivity and stability were determined and compared to bulk MOFs. Therefore, the progress of the humidity induced luminescence intensity quenching of the MMMs and the corresponding bulk substances was investigated for several pre-set relative humidities at room temperature. The MMMs show distinct and diverse luminescence loss and sensitivity rendering the monitoring of a very low relative humidity of only 2% accessible.

Introduction

Many processes in technical fabrications and chemical reactions have to be observed and monitored appropriately. Subsequent to production chains, storage conditions and transport challenges also apply to packaged materials. The translation of such processes, such as changes in the status of a system or in environmental parameters, to an observable value can be achieved with sensors and detectors.^{1–6} The detected parameters can be based on different processes such as suitable optical processes, for instance, changes in the intensity of luminescence such as “turn-on”⁷ or “turn-off” sensing⁸ or in energy and therefore chromaticity shifts of luminescence.⁹ Besides optical detection, several other physical processes, such as conductivity changes,¹⁰ magnetism¹¹ or chemical processes, such as changes in pH-values¹² or in ion concentrations,¹³ are used for sensing. The requirements for possible sensors are typically high sensitivity, defined threshold values, specificity, steadiness, fast reaction times and low costs. In order to avoid erroneous detection, sensing devices should be designed according to their respective application.¹⁴ Humidity, and thus water vapour, has a strong impact on packaged materials in face of world-wide transportation and day-to-day storage related

to the relative humidity of at least several percent, especially, if the materials have certain sensitivity to water. Here, sensing is possible chemically, *e.g.* based on classic cobalt salts^{15,16} but also on MOFs¹⁷ and lanthanide containing compounds.¹⁸ Physical humidity sensing is also possible based on optic behaviour (refractive index)¹⁹ or coulometric with *e.g.* the well-known Keidel cell.²⁰

The material groups of coordination polymers and especially metal–organic frameworks (MOFs) are known for their versatility, not only in structures²¹ but also in physical and chemical properties,²² including options for processing.²³ For two decades, MOFs are a research topic with a high priority now.²⁴ For luminescent MOFs and sensors, lanthanide-containing compounds (lanthanide-containing MOFs are called LnMOFs in the following) have mainly been investigated due to the possibility of an Ln³⁺-based intrinsic luminescence.^{25–27} As luminescence is a parameter that can be monitored “on-the-fly”, it is highly attractive for status analysis. By suitable combination of lanthanide ions and organic linkers, characteristic luminescence properties can be achieved,²⁸ including sensitization by light-harvesting organic ligands and metal-based emission.²⁹ In addition to typical 4f–Ln³⁺-systems, a few MOFs have been shown to utilize parity allowed, strong 5d–4f transitions for Eu²⁺ and Ce³⁺.³⁰ With the possibility of doping various amounts of lanthanides in different host lattices, different specific luminescence properties can be achieved in addition to the porosity of MOFs, which provides increased access for analyte molecules due to their additional inner surface. Both options make the material class of LnMOFs superior to *e.g.* Ln-complexes. Recently, particles of the MOF ${}^3_{\infty}[\text{Sr}_{0.90}\text{Eu}_{0.10}(\text{Im})_2]$ (2) have been embedded³¹ into a polysulfone

^a Institut für Anorganische Chemie, Universität Würzburg, Am Hubland, 97074 Würzburg, Germany. E-mail: k.mueller-buschbaum@uni-wuerzburg.de

^b Institut für Anorganische Chemie und Strukturchemie, Universität Düsseldorf, Universitätsstraße 1, 40225 Düsseldorf, Germany

† Electronic supplementary information (ESI) available: 13 figures and 3 tables on PL spectroscopy, PXRD, IR spectroscopy, elemental analysis, gas permeation, particle volume distribution, and SEM. See DOI: 10.1039/c8tc01454j

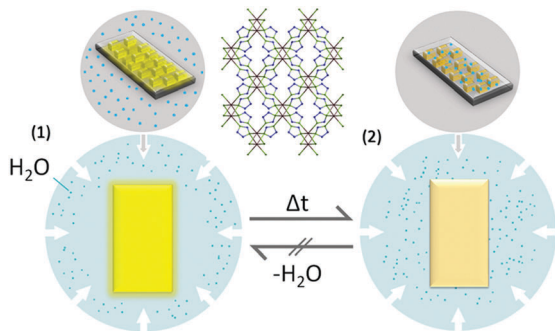


Fig. 1 Schematic presentation of the MMM sensing properties from the microscopic (upper part) to macroscopic (lower part) scale. Left: Luminescent MMM prior to the detection of humidity, right: quenched MMM-luminescence after sensing of humidity.

(PSF)³² matrix to create the first luminescent LnMOF mixed-matrix membranes (LnMOF@MMMs). Such embedding has also just been shown for luminescent Eu³⁺/Tb³⁺ complexes in poly(methylmethacrylate).³³

In this work, we have investigated the humidity sensitivity of different LnMOF@MMMs and their possible application as humidity sensors (Fig. 1). For applications such as transport or long-term storage, in which real status analysis is not based on 24 hour monitoring, irreversible detection is strongly preferable, as it prevents erroneous analysis based on non-continuous reversible sensing, which would result from several changes in humidity over time. Therefore, an experimental setup was created in which the loss of luminescence could be detected under defined and reproducible conditions for the MMMs described here which show irreversible luminescence changes upon contact with humidity. For a better understanding of the physical and chemical processes kinetic calculations were made and the accumulated recesses were analysed. The results were then compared to the properties of the bulk MOFs in order to analyse the influence of the polymer matrix and its gas permeation properties.

Results and discussion

Preparation and characterization of LnMOF@PSF MMMs and bulk MOFs

Successful membrane preparation of lanthanide imidazolate MOFs has been achieved for polysulfone (PSF) as an organic polymer material for ${}^3_{\infty}[\text{Ba}_{0.98}\text{Eu}_{0.02}(\text{Im})_2]$ and ${}^3_{\infty}[\text{Sr}_{0.90}\text{Eu}_{0.10}(\text{Im})_2]$, retaining the strong MOF luminescence. Relatively low loadings with the MOF as filler particles are preferable, as reported previously,³¹ and 8 wt% proved to be some kind of optimum regarding the properties of the MOF (luminescence intensity, distribution of particles) and the mechanical film stability and flexibility. Therefore, the embedding in this work was carried out with 8 wt% particles of the MOFs ${}^3_{\infty}[\text{Ba}_{0.98}\text{Eu}_{0.02}(\text{Im})_2]$ (1),³⁴ ${}^3_{\infty}[\text{Sr}_{0.90}\text{Eu}_{0.10}(\text{Im})_2]$ (2),³⁵ and ${}^3_{\infty}[\text{Ce}(\text{Im})_3\text{ImH}]\cdot\text{ImH}$ (3)³⁶ in PSF. The corresponding bulk substances were ball milled to equalize the particle size. Embedding resulted in the formation of membranes of the constitution ${}^3_{\infty}[\text{Ba}_{0.98}\text{Eu}_{0.02}(\text{Im})_2]\text{@PSF}$ (1@PSF) and ${}^3_{\infty}[\text{Sr}_{0.90}\text{Eu}_{0.10}(\text{Im})_2]\text{@PSF}$ (2@PSF). The generation of a

luminescent MMM of the constitution ${}^3_{\infty}[\text{Ce}(\text{Im})_3\text{ImH}]\cdot\text{ImH}\text{@PSF}$ (3@PSF) could not be achieved; as for the resulting films, no Ce-based luminescence could be detected and also no MOF reflections could be found by PXRD, leading to the conclusion that embedding of 3 was not successful but resulted in decomposition of the MOF.

The generated MMM films were investigated by a combination of photoluminescence spectroscopy, powder X-ray diffraction, SEM/EDX and *in situ* investigations of property changes upon interaction with pre-set relative humidities for sensing. The results were then compared to the properties of the bulk MOFs including potential sensing properties.

Photoluminescence spectroscopy

Both the co-doped MOFs of the formula ${}^3_{\infty}[\text{Ba}_{0.98}\text{Eu}_{0.02}(\text{Im})_2]$ (1) and ${}^3_{\infty}[\text{Sr}_{0.90}\text{Eu}_{0.10}(\text{Im})_2]$ (2) keep their luminescence properties unchanged upon embedding into the polysulfone matrix (PSF) as ${}^3_{\infty}[\text{Ba}_{0.98}\text{Eu}_{0.02}(\text{Im})_2]\text{@PSF}$ (1@PSF) and ${}^3_{\infty}[\text{Sr}_{0.90}\text{Eu}_{0.10}(\text{Im})_2]\text{@PSF}$ (2@PSF).³¹ It is worth mentioning that both archetype structures of ${}^3_{\infty}[\text{Ba}(\text{Im})_2]$, ${}^3_{\infty}[\text{Sr}(\text{Im})_2]$ and ${}^3_{\infty}[\text{Eu}(\text{Im})_2]$ are closely related, with the Ba-MOF being a distorted structure variant of the isotypic Sr- and Eu-MOFs.³⁵ Emission and excitation spectra were recorded at room temperature and compared to pure bulk MOFs. For both 1@PSF and 2@PSF, no deviation was observed between the emission of the bulk MOFs and the respective MMMs (Fig. 2).

This is an interesting feature, because different from typical Ln³⁺-intra-4f-based luminescence, the participation of 5d–4f transitions in the luminescence of Eu²⁺-ions should show energetic shifts if changes in the chemical surrounding apply. As this can be excluded, the fingerprint character of the photoluminescence (PL) already hints at embedding of chemically unchanged MOF particles that have little electronic interaction with the organic polymer. For 1, 2 and 1@PSF, 2@PSF, both excitation and emission are dominated by 5d–4f-transitions of Eu²⁺. However, in the excitation spectra, a certain bathochromic shift is caused by embedding into PSF.

Excitation at 365 nm leads to a strong yellow emission with a maximum at $\lambda = 555$ nm and a half width of about $\lambda = 105$ nm for 1 and 1@PSF. Also, data on the lifetimes of the Eu²⁺-emission for 1 and 1@PSF were collected and compared. Both cases can be described with a biexponential decay, which is also almost identical for the bulk MOF and the MMM ($\tau_1 = 215(3)$ ns and $\tau_2 = 450(8)$ ns, ($\lambda_{\text{exc.}} = 375$) for MOF 1 and $\tau_1 = 213(7)$ ns and $\tau_2 = 472(1)$ ns, ($\lambda_{\text{exc.}} = 375$ nm) for 1@PSF). Again, the strong similarities are a proof that the embedded MOF is unaltered. An according behaviour is observed for the photoluminescence properties of 2 and 2@PSF, which have been described recently,³¹ with identical photoluminescence properties for bulk MOF and MMM and a turquoise-green emission due to 5d–4f-transitions of Eu²⁺. Generation of an MMM of the constitution ${}^3_{\infty}[\text{Ce}(\text{Im})_3\text{ImH}]\cdot\text{ImH}\text{@PSF}$ (3@PSF) could not be proven, and the resulting films showed no Ce-based luminescence at all.

Powder X-ray diffraction, fluorescence microscopy, SEM and EDX

Subsequent to embedding, MMMs 1@PSF, 2@PSF and 3@PSF were further characterized *via* powder X-ray diffraction (PXRD),

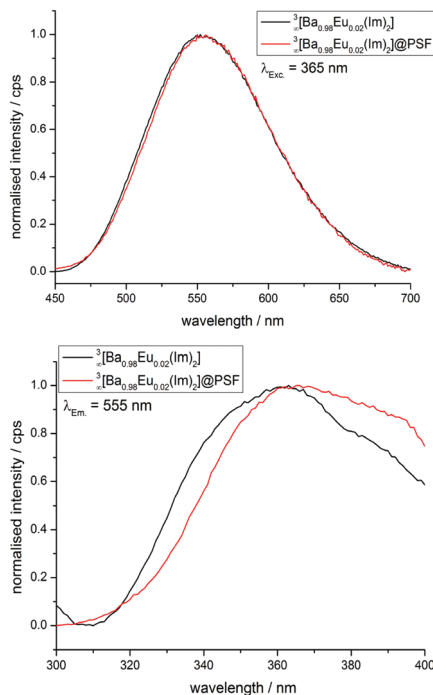


Fig. 2 Comparison of the emission (above) and excitation (below) spectra of bulk MOF **1** and MMM **1**@PSF with no difference being detected in emission.

fluorescence microscopy, scanning electron microscopy (SEM) and energy-dispersive X-ray spectroscopy (EDX). Unaltered MOF reflections could be detected in addition to the amorphous background of the organic polymer *via* PXRD for **1**@PSF and **2**@PSF (Fig. 3). However, no MOF reflections could be found for MMM **3**@PSF, leading to the conclusion that the embedding of **3** resulted in decomposition of the Ce-MOF instead. The decomposition can be recognized by a visible change in colour of the suspension, from grey to yellow as well as steady loss of the MOF luminescence, and starts upon stirring of the dispersion of the components. Removal of the solvent accelerates the decomposition (see also Fig. S11–S13, ESI[†]).

SEM together with EDX was applied to investigate the distribution of the MOF particles in the polymer membrane. The analysis shows a reasonably homogenous distribution of **1** in the matrix of the MMM **1**@PSF (Fig. 4), as can be seen by the distribution of the Ba²⁺ and Eu²⁺ ions over the complete area of the investigated MMM. An equally homogeneous distribution of **2** in **2**@PSF has been shown recently.³¹ Altogether, a homogenous luminescence on the macroscopic level can be seen by the eye if the MMMs are excited by UV-light ($\lambda_{\text{exc.}} = 365 \text{ nm}$, Fig. S1, ESI[†]). Sedimentation and aggregation are the result of decomposition of **3** in PSF.

Gas permeation

Gas permeation experiments have been conducted in order to determine whether the cast composite membranes were free of defects and without disturbances at the polymer–particle interface. Since the MOF filler is dense and does not exhibit

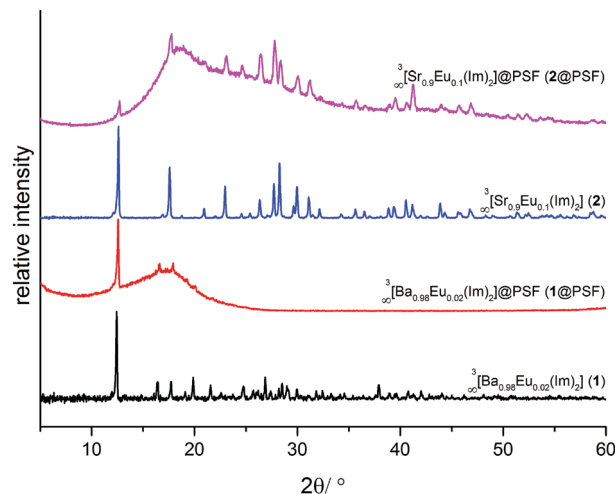


Fig. 3 Comparison of the observed powder X-ray diffraction patterns of MMMs **1**@PSF and **2**@PSF in comparison to the patterns of bulk MOFs **1** and **2**. The reflections of the MOFs and the amorphous background of the polymer matrix can be observed.

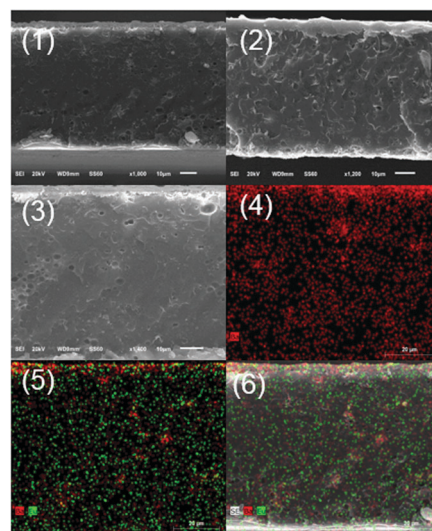


Fig. 4 (1–3) Cross-sectional SEM images of MMM **1**@PSF. (4–6) EDX elemental mapping for MMM showing the distribution of barium (red in 4–6) and europium (green in 5 and 6) in polysulfone. Image (6) includes image (1) together with EDX mapping.

porosity, its effect on the change in permeability of the membrane can be predicted using the Maxwell equation

$$P_c = P_m \cdot \frac{n \cdot P_f + (1 - n) \cdot P_m + (1 - n) \cdot (P_f - P_m) \cdot \phi_f}{n \cdot P_f + (1 - n) \cdot P_m - n \cdot (P_f - P_m) \cdot \phi_f}$$

wherein P_c , P_m and P_f are the permeabilities of the composite, pure polymer and filler, respectively, ϕ_f the volume fraction of the filler and n , a shape factor for the filler, in this case $n = 1/3$ for spherical particles.³⁹ Solving the equation for a non-porous filler, where $P_f = 0$, shows that the theoretical permeability through the MMM should be lower compared to the permeability of the pure polymer membrane. Dioxygen permeation experiments suggest that this is indeed the case for **1**@PSF and

Table 1 Gas permeation results^a

Membrane type	ϕ_f	$P_{O_2}(\text{exp.})$ [Barrer]	$P_c(\text{exp.})$ [Barrer]	$P_c(\text{calc.})$ [Barrer]	Relative deviation ^b
PSF	—	1.05	—	—	—
(1)@PSF	0.05	0.95	0.91	0.93	0.03
(2)@PSF	0.05	0.98	0.93	0.93	0.01

^a Individual values for different membranes for each MOF are given in Table S3 (ESI). ^b Relative deviation: $|(P_c(\text{exp.}) - P_c(\text{calc.}))/P_c(\text{calc.})|$.

for 2@PSF (Table 1). This confirms the assumption that the membranes are free of defects, as defects would have increased the permeability by allowing unhindered gas flux through the membrane.

Sensing properties of LnMOF@PSF MMMs in comparison to the bulk MOFs

For the detection of the quantitative luminescence decay during the sensing process, an experimental setup including a sample cell was built (Fig. 5). The sample cell consists of an inner and outer chamber, so that the outer chamber can only interact with the inner chamber, in which the MOF sample is placed, over the atmosphere in the hermetically sealed glass pipe. Humidity and temperature sensors were applied from the top. The outer chamber was filled with different cold saturated salt solutions to set a specific humidity value in the sample cell. Several salts were selected to reach the subsequent humidity levels of: LiCl for 12% rel. humidity, K(OOCCH₃) for 22%, K₂CO₃ for 42% and Mg(NO₃)₂ for 50% relative humidity. To avoid variation in the humidity values and the drying of the environment by the luminescent sample, the solutions were applied in excess so that *via* the evaporation equilibrium at constant humidity can be provided throughout all experiments at all time periods.

To keep the temperature constant, the chamber was placed in a temperature isolating box. After the humidity value reached equilibrium, the sample was exposed to this defined atmosphere, and the photoluminescence recording was started. Subsequently, the remaining samples were extracted and examined *via* X-ray powder diffraction and IR spectroscopy. Elemental analysis was carried out for the bulk substances.

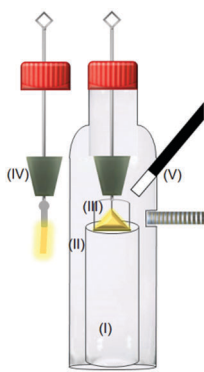


Fig. 5 Scheme of the sample cell for the sensing of humidity: the inner and outer chamber (I & II), the sample carrier (bulk MOF (III) or MMM (IV)) and attachment for the humidity and temperature sensor (V).

Sensing investigation of humidity on the bulk MOFs

If MOFs **1**, **2** and **3**³⁹ are exposed to humidity, a luminescence decay can be detected over time. This process can easily be visualised, if the collected emission spectra are plotted in a three dimensional arrangement with time as the *z*-axis, which is shown here for MOFs **1** and **2**, which were successfully embedded into PSF matrices 1@PSF and 2@PSF (Fig. 6). It is possible to describe these decay plots with the following exponential functions:

$$y = a \cdot \exp\left(-\frac{x}{t}\right) + y_0$$

$$y = A_1 \cdot \exp\left(-\frac{x}{t}\right) + A_2 \cdot \exp\left(-\frac{x}{t}\right) + y_0$$

y_0 = starting intensity, (MOFs), t = time (s), and y = intensity at the moment t (MOFs).

Due to the reservoir of saturated salt solution, a constant humidity can be provided leading to a decay which can kinetically be described as pseudo first order³⁷ behaviour. As anticipated, low humidity levels lead to a slower decay, which speeds up towards higher humidities. For all measurements, the reaction rate constant and half-life were calculated based on the fitted maxima of the 5d–4f transitions (555 nm (**1**) and 495 nm (**2**), (Table 2)). The calculated k' values were plotted against the concentration, which leads to a linear connection. The reaction rate constant for the overall humidity spectra can be anticipated from the slope of that line.

Although the two MOF systems appear to behave rather similar on the first glance, the luminescence decays vary in two points. First, the rate of the decay differs and based on it also the half-life, and second, the linear trend of the plotted k' values: for low humidity levels (12 or 22% rh), both MOFs show similar properties, and neither k' nor $t_{1/2}$ differ a lot between both systems. Above this point the decay of the luminescence of **2** is nearly six times faster than for **1**, which leads to a much shorter relative half-life (Fig. 7).

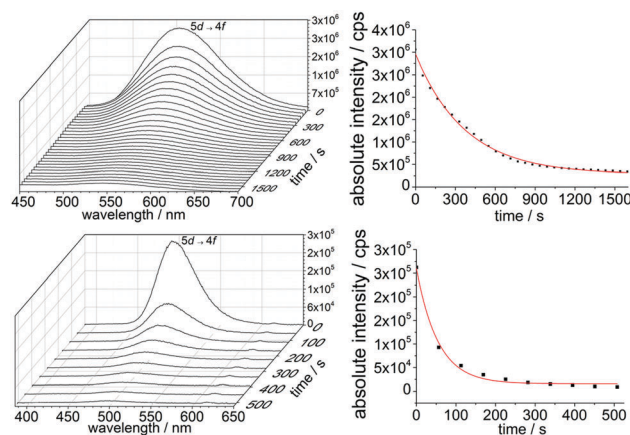


Fig. 6 3D-photoluminescence emission spectra of the collected time-intensity related data for ${}^3_2\text{Ba}_{0.98}\text{Eu}_{0.02}(\text{Im})_2$ (**1**, top) and ${}^3_2\text{Sr}_{0.90}\text{Eu}_{0.10}(\text{Im})_2$ (**2**, bottom), their corresponding courses of emission (left, excited at 365 and 366 nm, respectively) and the respective exponential fits (right) for 50% relative humidity (rh).

Table 2 Parameters of luminescence decay of MOFs for **1** and **2**^a

${}^3[\text{Ba}_{0.98}\text{Eu}_{0.02}(\text{Im})_2]$, 1	Kinetic (k') (s^{-1})	Half-life ($t_{1/2}$) (s)
12% rh	$2.0 \times 10^{-4} \pm 0.4 \times 10^{-4}$	2360 ± 643
22% rh	$3.1 \times 10^{-4} \pm 0.2 \times 10^{-4}$	1540 ± 158
50% rh	$30.0 \times 10^{-4} \pm 2.0 \times 10^{-4}$	286 ± 10
${}^3[\text{Sr}_{0.90}\text{Eu}_{0.10}(\text{Im})_2]$, 2	Kinetic (k') (s^{-1})	Half-life ($t_{1/2}$) (s)
12% rh	$1.4 \times 10^{-4} \pm 0.4 \times 10^{-4}$	3055 ± 132
22% rh	$43.0 \times 10^{-4} \pm 0.1 \times 10^{-4}$	1193 ± 200
50% rh	$170 \times 10^{-4} \pm 1 \times 10^{-4}$	39 ± 3

^a Deviation was calculated based on the experimental variance of the determined parameter for k' .

Based on these experimental results, it was possible to calculate the rate constant for the whole humidity range at 25 °C (Fig. 8). Both MOFs do not show the ideal behaviour, in which the plotted k' values should be located on a line crossing the origin. In the ideal case, the decay should start at atmospheric water concentrations close to zero. The actual linear fits ($y = ax + b$) cross the x -axis at water concentrations, which were calculated based on humidity and temperature, of 0.3 mmol L^{-1} for **1** and 0.14 mmol L^{-1} for **2**. Those intersections define the threshold values of the MOF systems, at which it can be reasonably used as sensors. An unusual observation was made for **1**: no intersection with the x -axis could be observed but a convergence below 17% rh. As a result, it is possible to identify two threshold values based on the different behaviour of the luminescence decay. For rather short

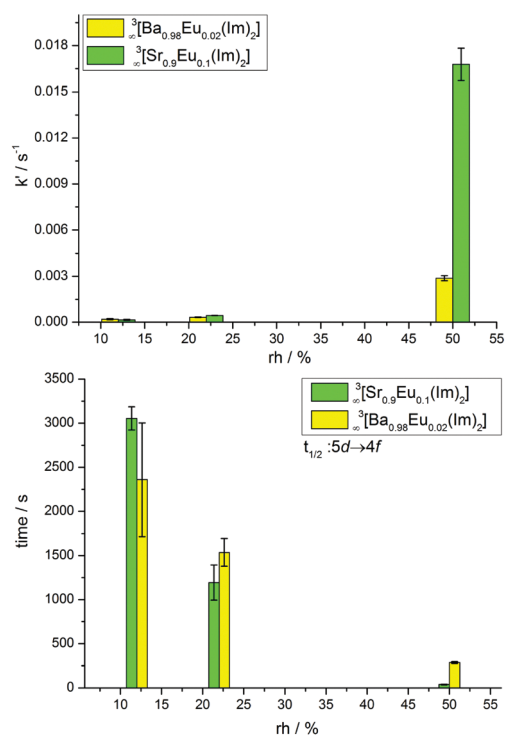


Fig. 7 Comparison of the k' values (above) and the half-life (below) of the bulk MOFs **1** (yellow bars) and **2** (green bars) at different relative humidity (rh) levels.

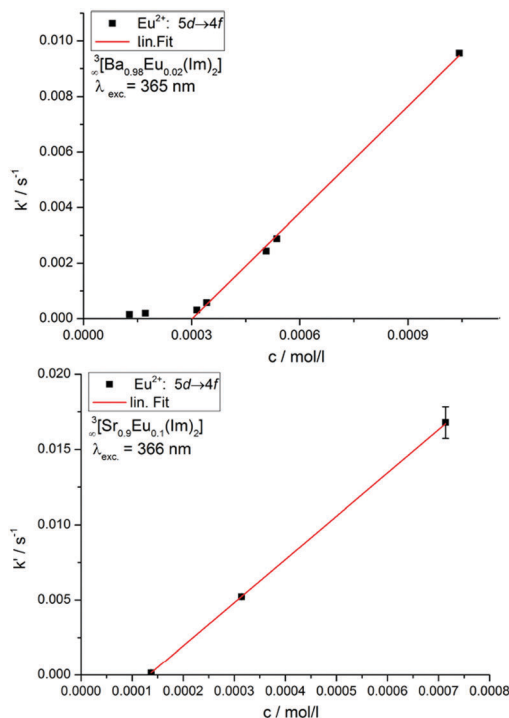


Fig. 8 Plot of the k' values of the luminescence decay of **1** (above) and **2** (below). In contrast to **2**, the k' values of **1** do not follow one linear function, but also a second almost linear function below 17% rh with a smaller slope.

periods of observation times, a threshold after the intersection of the linear fit with the x -axis applies, for which the rate of the decay rises and shortens the detection time to a few minutes (ideal for “on-the-fly”-real status determination) resulting in a threshold value of 10% rh for **2** and 25% rh for **1**.

However, it is possible to detect a lower limit of relative humidity from 2% rh (extrapolation) for **2** by the very slow decay over a long time (hours to days, ideal for storage), resulting in a significant difference of the MOFs **1** and **2** (Fig. 8).

Sensing investigations of humidity for MMMs of LnMOF@PSF

The corresponding MMMs ${}^3[\text{Ba}_{0.98}\text{Eu}_{0.02}(\text{Im})_2]$ @PSF (**1**@PSF) and ${}^3[\text{Sr}_{0.90}\text{Eu}_{0.10}(\text{Im})_2]$ @PSF (**2**@PSF) were investigated in the same way as the bulk MOFs in order to allow a direct comparison of the sensing properties. An investigation of **3**@PSF was omitted due to the lack of significant luminescence. The respective 3D-photoluminescence spectra and plots of the kinetics of decay are depicted in Fig. 9. As expected, the MMMs show a different behaviour than the bulk MOFs (see Table 3).

A closer look on the data reveals expected and unexpected results. The embedding of **1** in the PSF membrane leads to an overall higher stability of the MOF particles in **1**@PSF. As expected, the luminescence decay is slowed down, overall, $t_{1/2}$ values are getting higher for the MMMs and the decay cannot be described with a single function, anymore, but consists of two different kinetic processes (Fig. 10). This reflects that the permeation and the water interaction of the bulk particles have a different reaction rate. Consequently, this results in an

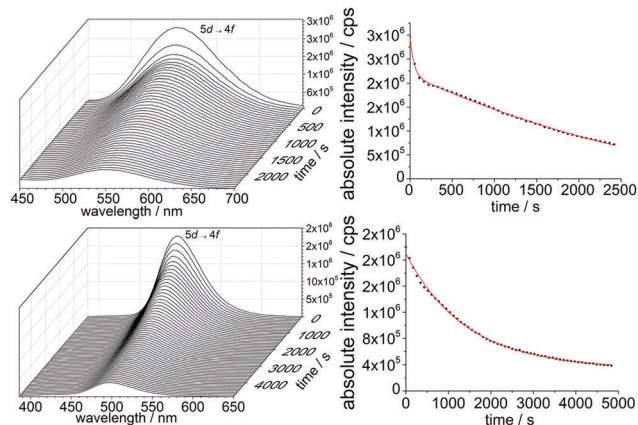


Fig. 9 3D-photoluminescence emission spectra of the collected time-intensity related data for ${}^3\text{Ba}_{0.98}\text{Eu}_{0.02}(\text{Im})_2$ @PSF (**1**@PSF, top) and ${}^3\text{Sr}_{0.90}\text{Eu}_{0.10}(\text{Im})_2$ @PSF (**2**@PSF, bottom), their corresponding courses of emission (left, excited at 365 and 366 nm, respectively) and the respective exponential fits (right) for 50% relative humidity (rh).

Table 3 Parameters for luminescence decay of **1**@PSF and **2**@PSF^a

${}^3\text{Ba}_{0.98}\text{Eu}_{0.02}(\text{Im})_2$ @PSF, 1 @PSF	Kinetic (k_1') (s^{-1})	Half-life ($t_{1/2}$) (s)
12% rh	$33 \times 10^{-4} \pm 8 \times 10^{-4}$	222 ± 52
42% rh	$66 \times 10^{-4} \pm 2 \times 10^{-4}$	106 ± 2
50% rh	$225 \times 10^{-4} \pm 2 \times 10^{-4}$	31 ± 3
	Kinetic (k_2') (s^{-1})	Half-life ($t_{1/2}$) (s)
12% rh	$3.0 \times 10^{-4} \pm 0.7 \times 10^{-4}$	2454 ± 571
42% rh	$4.9 \times 10^{-4} \pm 0.3 \times 10^{-4}$	1433 ± 85
50% rh	$2.7 \times 10^{-4} \pm 0.3 \times 10^{-4}$	2642 ± 285
${}^3\text{Sr}_{0.90}\text{Eu}_{0.10}(\text{Im})_2$ @PSF, 2 @PSF	Kinetic (k_1') (s^{-1})	Half-life ($t_{1/2}$) (s)
12% rh	$1.5 \times 10^{-4} \pm 0.1 \times 10^{-4}$	4616 ± 406
22% rh	$4.5 \times 10^{-4} \pm 0.1 \times 10^{-4}$	1529 ± 21
50% rh	$7.1 \times 10^{-4} \pm 0.1 \times 10^{-4}$	973 ± 17

^a Deviation was calculated based on the experimental variance of the determined parameter for k' .

increase of the stability of the MOFs in the MMMs and thereby also better processability of the films in potential applications compared to the bulk MOFs. The gas molecules can now no longer directly affect the MOF but are influenced by the permeation properties of the films, as they need to permeate through the organic polymer matrix in order to reach the MOF.

However, this also implies that a possible sensing process is influenced by the permeation of the analyte through the film, which requires additional time. This extends the time scale for MOF-luminescence intensity changes from minutes to hours, although the recording of spectra itself remains equally fast. In principle, this increase on the detection time scale is not a problem for the monitoring of long-term storage, as the latter is based on many hours rather than minutes. Also, the threshold value for the MOF hydrolysis is shifted to lower concentrations (intersection with x -axis at 0.1 mmol L^{-1} , Fig. 11), as a certain hydrophilic nature of the membrane together with constant

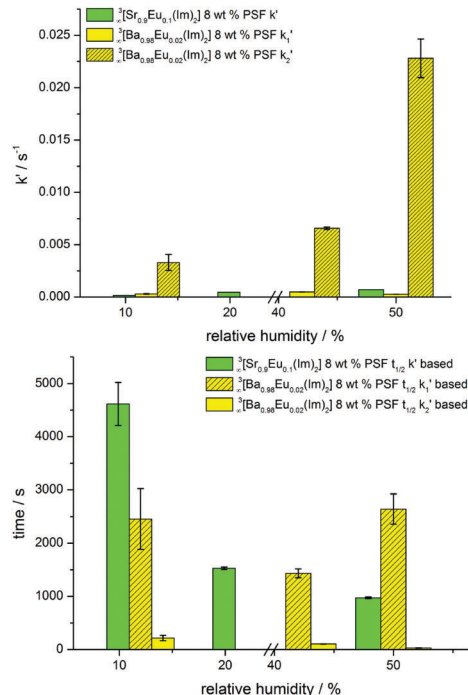


Fig. 10 Comparison of the k' values (above) and the half-life (below) of **1**@PSF (yellow bars) and **2**@PSF (green bars) at different relative humidity (rh) levels.

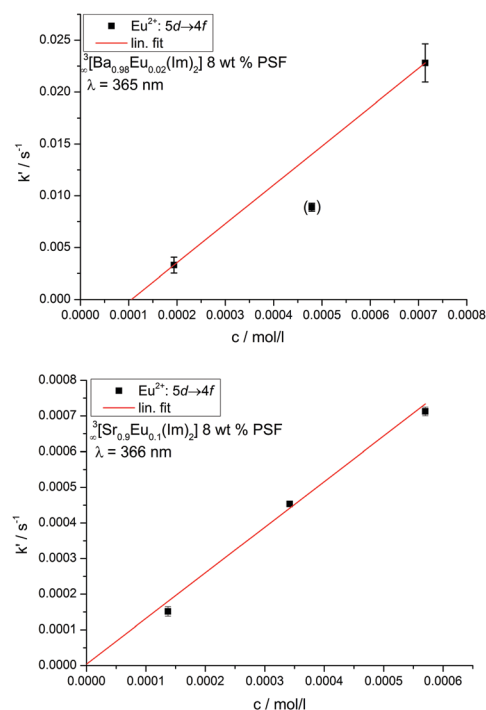


Fig. 11 The plotted k' values of **1**@PSF (above) and **2**@PSF (below), and the latter showing ideal behaviour by crossing the origin.

supply of humidity allows for a preconcentration effect influencing the detection over a long time and influencing the sensitivity. Deviation in MMM permeation may also result from different thicknesses of the MMM sensor membrane.

The properties of MMMs of type 2@PSF differ from MMM 1@PSF. In contrast to 1@PSF, the luminescence decay of 2@PSF can be described with one function leading to the assumption that the two processes (gas permeation and hydrolysis) have approximately equal rates. The overall stability of the embedded MOF particles is 1.5 times higher for 12% rh and nearly 4 times higher for 50% rh, leading to a half-life of 4616(405) s for 12% rh. The main difference of 2@PSF to 1@PSF but also to the bulk experiments is that the threshold value extrapolated from the linear fit shows ideal behaviour by crossing the origin.

PXRD, infrared spectroscopy and elemental analysis

Prior to and subsequent to the sensing experiments, samples of the MOFs and the respective MMMs were investigated by several analytic methods. Each sample was investigated by PXRD and IR spectroscopy; MOF bulk samples were also analysed *via* elemental analysis for their CHN content. Furthermore, a comparison of powder X-ray diffraction of the MMMs and the respective bulk MOFs was carried out (Fig. S6, ESI[†]).

For bulk MOF 1, even for low humidity levels ($\geq 12\%$ rh), reflections of imidazole can be found pointing towards protonation of the anionic ligands. As a trend, these intensities increase at higher humidity ($\geq 22\%$ rh). At high humidity levels ($\geq 50\%$ rh), the powder pattern consists of imidazole, Ba(OH)₂ and small reflection intensities of bulk MOF, indicating the hydrolysis of the MOF. In contrast to these findings, $^3\text{[Ba}_{0.98}\text{Eu}_{0.02}(\text{Im})_2]\text{@PSF}$ membranes 1@PSF only show the MOF reflections for 12% rh. It is possible that due to the rigid structure of the organic polymer matrix, released imidazole cannot crystallize inside the polymer film, so that none of its reflections appear. For high humidities ($> 42\%$ rh), reflections of Ba(OH)₂ can be detected, corroborating the interpretation of the hydrolysis process, as found for the bulk MOF at 50% rh.

MOF $^3\text{[Sr}_{0.90}\text{Eu}_{0.10}(\text{Im})_2]$ (2) and its MMM 2@PSF were also investigated according to a previous description (Fig. S7, ESI[†]). For low humidity levels ($\leq 12\%$ rh), both MMM and bulk material show no differences to the corresponding starting material, indicating that changes are too limited to be observable by PXRD. Raising the humidity level to 22% rh leads to slight changes in the pattern of both 2 and 2@PSF, showing additional reflections that can be found in addition to the reflections of 2 and imidazole. Hence, the anionic ligand is protonated, released and an additional unknown crystalline phase is formed during sensing, corroborating the assumption of an irreversible detection process. The main reflection of this phase can be seen in the MMM pattern 2@PSF for 50% rh. Due to the character of the surrounding organic film, no large crystalline growth inside the MMM is possible, leading to weaker intensities of the reflections compared to the bulk MOF. For the highest humidity level tested (50% rh), the powder pattern of 2@PSF exhibits no MOF reflections of 2 but reflections of Sr(OH)₂ and the already mentioned unknown phase, again indicating hydrolysis as the base of the irreversible detection.

IR-spectroscopy is another useful method to detect vibrational groups including OH, water, N–H of imidazole or potential species that may not be found by PXRD, as they may be non-crystalline or too low in amount. For 1 and 2 (Fig. S7 and S9, ESI[†]) at low

humidity levels (12–22% rh), very weak bands of the N–H stretching vibration between 3500 and 3300 cm⁻¹ are found. For 50% rh free imidazole dominates the spectrum in addition to two OH related bands at 3305 cm⁻¹ and 3608 cm⁻¹. For membranes 1@PSF and 2@PSF, no changes in the IR spectra can be detected at 12% rh, and only slight changes appear at 22% rh (weak bands at 2918 and 2850 cm⁻¹ belonging to imidazole). A significant change in the pattern of the IR spectra of 1@PSF can be observed at 50% rh, and at this humidity level the fingerprint region is dominated by broad and diffuse bands. For membrane 2@PSF at 50% rh, only the bands of imidazole can be detected. Typical N–H vibrations appear, and the bathochromic shift of bonded imidazolate vanishes, both prove that during the hydrolysis process imidazole is released.

To check the amount of water that was taken up by the MOFs during the sensing process, the bulk MOFs were also checked *via* elemental analysis and based on the changes in the amount of carbon the amount of water was calculated (0–2 equivalents for 1 and 0–5.5 equivalents for 2) (Table S1, ESI[†]). It can be seen that for both 1 and 2, the amount of water increases for higher humidity levels. Unfortunately, the high and not specifically defined organic content and therefore the elemental composition of MMMs prohibit suitable CHN analysis of the MMMs.

Conclusion

Mixed matrix membranes were generated from luminescent co-doped alkaline earth/lanthanide imidazolate MOFs and poly-sulfone. Sensitive sensor MMMs were generated that exceed bulk MOFs in stability, handling and long-term monitoring, which can be especially interesting for overseas transport or long-term storage under atmospheric conditions (rh of several percent) whilst retaining the general sensitivity of the sensing process. Three highly luminescent Ln-imidazolate MOFs $^3\text{[Sr}_{0.90}\text{Eu}_{0.10}(\text{Im})_2]$, $^3\text{[Ba}_{0.98}\text{Eu}_{0.02}(\text{Im})_2]$ and $^3\text{[Ce}(\text{Im})_3\text{ImH]ImH}$ were investigated, of which the Sr/Eu and Ba/Eu combinations gave luminescent membranes by embedding of the unchanged MOFs. The product MMMs were investigated for potential humidity sensing and the results were compared to the sensing properties of the bulk MOFs for several pre-set humidity values including a study of the kinetics of the sensing processes. To the best of our knowledge, these are the first luminescence sensing investigations with MOF containing membrane systems. The bulk MOFs and especially the membranes exhibit sensing of humidity starting at 2% rel. humidity, observable by quenching of the MOF luminescence as a function of the water concentration. Due to the gas permeation through the organic polymer, the membranes show slower detection compared to the bulk MOFs but also improved stability towards air and therefore better processability in potential applications, as they can be handled in a normal atmosphere – different to the MOFs themselves. As the delay in monitoring caused by the permeation processes is no issue for real status analysis of long-term processes, the stability increase is strongly favourable, and the error free character of

irreversible detection if preferable over reversible sensing in all cases that do not allow for 24/7 monitoring.

The detection process was monitored *in situ* to the interaction of the sensor system and the analyte and was characterized as ongoing hydrolysis. Permeation experiments have verified that the membranes are free of defects. The calculated theoretical permeabilities for the mixed matrix membranes show little deviation from the measured permeabilities.

Altogether, it was possible to show that MMMs can be used as sensors or detectors for different levels of humidity and time scales, and the occurring luminescence decay can also be kinetically and mathematically described. It can be shown that embedding of MOF particles influences the detection sensitivity to lower reaction rate constants and can change the threshold value for the selected MOF, creating design space for selective adaption of LnMOF based sensors for highly specific applications. Overall, the presented results can open a pathway to long term sensing *via* luminescence in mixed matrix membrane systems.

Experimental section

For general experimental considerations, please see the ESI.†

Synthesis of ${}^3_{\infty}[\text{Ba}_{0.98}\text{Eu}_{0.02}(\text{Im})_2]$ (1)

The MOF was synthesised according to the literature.³⁴ The gained product was a yellow fine powder of **1**. Yield: 350.66 mg = 87%. Anal. calcd for $\text{C}_6\text{H}_6\text{N}_4\text{Ba}_{0.98}\text{Eu}_{0.02}$ ($M_r = 205.70 \text{ g mol}^{-1}$): C, 26.52%; N, 20.61%; H, 2.95%. Found: C, 26.89%; N, 19.78%; H, 2.23%.

Synthesis of ${}^3_{\infty}[\text{Sr}_{0.90}\text{Eu}_{0.10}(\text{Im})_2]$ (2)

Substance **2** was synthesised according to the literature.³⁵ The product was gained as a yellow crystalline powder. Yield: 203.02 mg = 89%; anal. calcd for $\text{C}_6\text{H}_6\text{N}_4\text{Sr}_{0.9}\text{Eu}_{0.10}$ ($M_r = 228.21 \text{ g mol}^{-1}$): C, 31.58%; N, 24.55%; H, 2.65%. Found: C, 32.26%; N, 24.24%; H, 2.84%.

Synthesis of ${}^3_{\infty}[\text{Ce}(\text{Im})_3\text{ImH}]\cdot\text{ImH}$ (3)

Substance **3** was synthesised according to the literature.³⁹ The gained product was a greyish fine powder of **3**. Yield: 368.4 mg = 90% anal. calcd for $\text{CeC}_{15}\text{H}_{17}\text{N}_{10}$ ($M_r = 477.48 \text{ g mol}^{-1}$): C, 37.73%; N, 29.33%; H, 3.59%. Found: C, 36.95%; N 28.22%; H 3.68%.

Membrane preparation (1@PSF–3@PSF)

Before embedding into the polymer, the MOFs were ground in a ball mill under argon to adjust the particle size to about 50 μm for (**1**) (Fig. S11, ESI†) (150 s at 15 Hz). Portions (200 mg) of the dry polymer, the MOF material (18 mg), and dry dichloromethane (4 mL) were combined in a 10 mL Schlenk flask to produce MMMs with 8 wt% of the respective MOFs **1–3**. The dispersions were stirred for 2 d in order to achieve homogeneous mixtures and were cast into metal rings, 5 cm in diameter, which were placed on a flat glass surface in a desiccator filled with nitrogen gas and a desiccant. The solvent was evaporated

overnight by a slight stream of pre-dried nitrogen gas to ensure a sufficient evaporation rate. As soon as all of the solvent was evaporated, the membrane was removed from the metal ring and the glass surface. The membrane was finally dried at 25 °C under reduced pressure.

For details on the powder X-ray diffraction (PXRD) analyses, please check the ESI.†

For details on the SEM/EDX analyses, please see the ESI.†

Photoluminescence spectroscopy

Excitation and emission spectra were recorded with a Horiba Jobin Yvon Fluorolog 3 photoluminescence spectrometer with a 450 W Xe lamp, Czerny–Turner double grating (1200 grooves per mm) excitation and emission monochromators and an R928P detector. Emission spectra range from 400 to 680 nm and were corrected for the spherical response of the monochromators and the detector using typical correction spectra. Excitation spectra were recorded from 300 to 400 nm and corrected for the spectral distribution of the lamp intensity using a photodiode reference detector.

The overall luminescence process lifetimes of the MMM **2**@PSF and of the films **1**@PSF and **2**@PSF subsequent to sensing were obtained by determination of the luminescence decay with a Horiba Fluoromax FL3-22 spectrophotometer. Samples were prepared in quartz glass cuvettes under an inert-gas atmosphere, and the decay times were recorded by time-correlated single-photon counting (TCSPC) with a 375 nm pulsed laser diode or a microsecond flash lamp with an excitation wavelength of 330 nm. The fluorescence emission was collected at right angles to the excitation source, and the emission wavelength was selected with a monochromator and detected using a single-photon avalanche diode (SPAD). The resulting intensity decays were calculated through tail fits.

Gas permeation

The O_2 permeabilities were evaluated with a permeation cell described elsewhere.³⁸ The membrane thickness was measured as the average over ten different spots with a micrometer screw. The gas permeation measurements were performed using the pressure-rise method under steady-state conditions at 30 °C. The membrane was placed into the sample cell; permeate and feed sides were evacuated. The feed side was filled with O_2 gas to a pressure of 3.0 bar. The linear pressure increase upon permeation from the feed to the permeate side was recorded and used to calculate the permeability P in Barrer units [1 Barrer = $1 \times 10^{-10} \text{ cm}^3$ (STP) $\text{cm} (\text{cm s cmHg})^{-1}$ or $7.5005 \times 10^{-18} \text{ m}^2 \text{ s}^{-1} \text{ Pa}^{-1}$ in SI units]. Permeability P is defined as gas flow rate J multiplied by thickness d of the membrane, divided by area A and by pressure difference Δp across the material:

$$P = (J \cdot d) / \Delta p \cdot A$$

For the Maxwell equation, assumed shape factor n was 1/3, as it is commonly used for spherical particles. The density of the polymer was taken from the material data sheet, the density of the fillers were calculated from the crystal structures, permeability P_f of the filler was assumed to be 0 for a non-porous

material and permeability P_m of the pure polymer was measured under the same conditions in the same permeation cell as those in the MMMs.^{35,40,41}

Sensing/detection investigations

For the sensing experiments of the bulk MOFs, 7.0 mg (0.034 mmol) of $^3\text{Ba}_{0.98}\text{Eu}_{0.02}(\text{Im})_2$ (1) or 7.0 mg (0.030 mmol) of $^3\text{Sr}_{0.90}\text{Eu}_{0.10}(\text{Im})_2$ (2), respectively, were placed in a sample cell consisting of a reservoir for different saturated salt solutions, a hygrometer and the hermetically closed sample carrier. The cell was filled under inert conditions to avoid premature hydrolysis. After the sample carrier was capped, the reservoir was filled with 80 mL of saturated salt solutions adjusting different, constant humidity values, which were equilibrated ($\text{LiCl} \approx 12\%$, $\text{K}(\text{CH}_3\text{COO}) \approx 22\%$, $\text{K}_2\text{CO}_3 \approx 42\%$ and $\text{Mg}(\text{NO}_3)_2 \approx 50\%$). Humidity and temperature in the sample cell were monitored with a humidity and temperature sensor. The sample was exposed to a defined humidity-containing atmosphere and simultaneously the recording of the emission spectra was started. For the measurement of the MMMs, the films were fixed with a clip in the hermetically closed sample carrier. In both cases, emission spectra were recorded every 30 s. The measuring cell was coupled with a Horiba Fluorolog-3 photoluminescence spectrometer *via* a fibre-optic cable.

Humidity detection

For the *in situ* humidity detection a Testo 645 humidity and temperature measuring device was used with a temperature and humidity detector capped with a PTFE cap. The device is able to detect humidity and temperature in the range of 0–100(2)% rh from -20 to $70(2)^\circ\text{C}$.

Elemental analysis

The bulk materials of 1–3 were investigated using elemental analysis for C, H and N, before and after the hydrolysis process, performed with an ELEMENTAR Vario El CHN analyser.

Vibrational spectroscopy

FTIR spectra were recorded using a Thermo Nicolet FTIR-380 spectrometer.

Conflicts of interest

There are no conflicts to declare.

Acknowledgements

We gratefully acknowledge support from the Volkswagen Stiftung within the project “Multifunctional Molecular Materials”.

References

- L. G. Qiu, Z. Q. Li, Y. Wu, W. Wang, T. Xu and X. Jiang, *Chem. Commun.*, 2008, 3642–3644.
- Z. Xie, L. Ma, K. E. de Krafft, A. Jin and W. J. Lin, *J. Am. Chem. Soc.*, 2009, **132**, 922–923.
- Q. Tan, J. Liu and Z. Liu, *Dalton Trans.*, 2016, **45**, 18450–18454.
- Z. Chen, J. Chen and D. Pan, *Anal. Bioanal. Chem.*, 2017, **409**, 2429–2435.
- C. Zhi and C. Lu, *Sens. Lett.*, 2005, **4**, 274–295.
- L. E. Kreno, K. Leong, O. K. Farha, M. Allendorf, R. P. Van Duyne and J. T. Hupp, *Chem. Rev.*, 2012, **112**, 1105–1125.
- D. K. Singha and P. Mahata, *Inorg. Chem.*, 2015, **54**, 6373–6379.
- S. Bhattacharyya, A. Chakraborty, K. Jayaramulu, A. Hazra and T. K. Maji, *Chem. Commun.*, 2014, **50**, 13567–13570.
- H. Lee, S. H. Jung, W. S. Han, J. H. Moon, S. Kang, J. Y. Lee, J. H. Jung and S. Shinkai, *Chem. – Eur. J.*, 2011, **17**, 2823–2827.
- G. Lu, O. K. Farha, L. E. Kreno, P. M. Schoenecker, K. S. Walton, R. P. Van Duyne and J. T. Hupp, *Adv. Mater.*, 2011, **23**, 4449–4452.
- E. Coronado and G. Mínguez Espallargas, *Chem. Soc. Rev.*, 2013, **42**, 1525–1539.
- H. Y. Li, Y. L. Wei, X. Y. Dong, S. Q. Zang and T. C. W. Mak, *Chem. Mater.*, 2015, **27**, 1327–1331.
- B. Chen, L. Wang, Y. Xiao, F. R. Fronczek, M. Xue, Y. Cui and G. Qian, *Angew. Chem.*, 2009, **121**, 508–511 (*Angew. Chem., Int. Ed.*, 2009, **48**, 500–503).
- X. S. Wang, L. Li, D. Q. Yuan, Y. B. Huang and R. Cao, *J. Hazard. Mater.*, 2017, **16**(344), 283–290.
- F. Boltinghouse and K. Abel, *Anal. Chem.*, 1989, **61**, 1863–1866.
- A. Tsigara, G. Mountrichas, K. Gatsouli, A. Nichelatti, S. Pispas, N. Madamopoulos, N. A. Vainos, H. L. Du and F. Roubani-Kalantzopoulou, *Sens. Actuators, B*, 2007, **120**, 481–486.
- (a) A. Weiss, N. Reimer, N. Stock, M. Tiemann and T. Wagner, *Microporous Mesoporous Mater.*, 2016, **220**, 39–43; (b) Y. Yu, X. Zhang, J. Ma, Q. Liu, P. Wang and Y. Dong, *Chem. Commun.*, 2014, **50**, 1444–1446; (c) J. Wu and B. Yan, *Dalton Trans.*, 2017, **46**, 7098–7105; (d) D. Wang, Q. Tan, J. Liu and Z. Liu, *Dalton Trans.*, 2016, **45**, 18450–18454; (e) L. V. Meyer, F. Schönfeld, A. Zurawski, M. Mai, C. Feldmann and K. Müller-Buschbaum, *Dalton Trans.*, 2015, **44**, 4070–4079; (f) F. Wang, Y.-T. Wang, H. Yu, J.-X. Chen, B.-B. Gao and J.-P. Lang, *Inorg. Chem.*, 2016, **55**, 9417–9423.
- F. Y. Yi, D. Chen, M. K. Wu, L. Han and H. L. Jiang, *ChemPlusChem*, 2016, **81**, 675–690.
- D. Gomez, S. P. Morgan, B. R. Hayes-Gill, R. G. Correia and S. Korposh, *Sens. Actuators, B*, 2018, **254**, 887–895.
- F. A. Keidel, *Anal. Chem.*, 1959, **31**, 2043–2048.
- O. M. Yaghi, *Acc. Chem. Res.*, 2010, **43**, 58–67.
- (a) O. K. Farha and J. T. Hupp, *Acc. Chem. Res.*, 2010, **43**, 1166–1175; (b) C. Janiak and S. K. Henninger, *Chimia*, 2013, **67**, 419–424; (c) S. K. Henninger, F. Jeremias, H. Kummer and C. Janiak, *Eur. J. Inorg. Chem.*, 2012, 2625–2634; (d) F. P. Doty, C. A. Bauer, A. J. Skulan, P. G. Grant and M. D. Allendorf, *Adv. Mater.*, 2009, **21**, 95–101; (e) H. Lee, S. H. Jung, W. S. Han, J. H. Moon, S. Kang, J. Y. Lee, J. H. Jung and S. Shinkai, *Chem. – Eur. J.*, 2011, **17**, 2823–2827.
- P. Falcaro, R. Ricco, C. M. Doherty, K. Liang, J. A. Hill and M. J. Styles, *Chem. Soc. Rev.*, 2014, **43**, 5513–5560.

- 24 H. C. Zhou, J. R. Long and O. M. Yaghi, *Chem. Rev.*, 2012, **112**, 673–674.
- 25 (a) S. Roy, A. Chakraborty and T. K. Maji, *Coord. Chem. Rev.*, 2014, **273**, 139–164; (b) L. V. Meyer, F. Schönfeld and K. Müller-Buschbaum, *Chem. Commun.*, 2014, **50**, 8093–8108; (c) Y. Cui, B. Chen and G. Qian, *Chem. Rev.*, 2014, **273**, 76–86; (d) L. Ma, O. R. Evans, B. M. Foxman and W. Lin, *Inorg. Chem.*, 1999, **38**, 5837–5840; (e) T. M. Reinecke, M. Eddaoudi, M. Fehr, D. Kelly and O. M. Yaghi, *J. Am. Chem. Soc.*, 1999, **121**, 1651–1657; (f) Z. S. Bai, J. Xu, T. Okamura, M. S. Chen, W. Y. Sun and N. Ueyama, *Dalton Trans.*, 2009, 2528–2539.
- 26 (a) Y. Xiao, Y. Cui, Q. Zheng, S. Xiang, G. Qian and B. Chen, *Chem. Commun.*, 2010, **46**, 5503–5505; (b) Z. Guo, H. Xu, S. Su, J. Cai, S. Dang, S. Xiang, G. Qian, H. Zhang, M. O’Keeffe and B. Chen, *Chem. Commun.*, 2011, **47**, 5551–5553.
- 27 T. Wehner, M. T. Seuffert, J. R. Sorg, M. Schneider, K. Mandel, G. Sxtdl and K. Müller-Buschbaum, *J. Mater. Chem. C*, 2017, **5**, 10133–10142.
- 28 K. Müller-Buschbaum, F. Beuerle and C. Feldmann, *Micro-porous Mesoporous Mater.*, 2015, **216**, 171–199.
- 29 K. Binnemans, *Chem. Rev.*, 2009, **109**, 4283–4374.
- 30 L. V. Meyer, F. Schönfeld, A. Zurawski, M. Mai, C. Feldmann and K. Müller-Buschbaum, *Dalton Trans.*, 2015, **44**, 4070.
- 31 J. Dechnik, F. Mühlbach, D. Dietrich, T. Wehner, M. Gutmann, T. Lühmann, L. Meinel, C. Janiak and K. Müller-Buschbaum, *Eur. J. Inorg. Chem.*, 2016, 4408.
- 32 (a) J. Won, J. S. Seo, J. H. Kim, H. S. Kim, Y. S. Kang, S. J. Kim, Y. Kim and J. Jegal, *Adv. Mater.*, 2005, **17**, 80–84; (b) A. Car, C. Stropnik and K. V. Peinemann, *Desalination*, 2006, **200**, 424–426; (c) B. Seoane, J. M. Zamaro, C. Tellez and J. Coronas, *RSC Adv.*, 2011, **1**, 917–922; (d) B. Zornoza, B. Seoane, J. M. Zamaro, C. Tellez and J. Coronas, *Chem-PhysChem*, 2011, **12**, 2781–2785.
- 33 D. Yang, D. Liu, C. Tian, S. Wang and H. Li, *J. Colloid Interface Sci.*, 2018, **519**, 11–17.
- 34 J. C. Rybak, M. Hailmann, P. R. Matthes, A. Zurawski, J. Nitsch, A. Steffen, J. G. Heck, C. Feldmann, S. Götzendörfer, J. Meinhardt, G. Sxtdl, H. Kohlmann, S. J. Sedlmaier, W. Schnick and K. Müller-Buschbaum, *J. Am. Chem. Soc.*, 2013, **135**, 6896–6902.
- 35 (a) A. Zurawski, M. Mai, D. Baumann, C. Feldmann and K. Müller-Buschbaum, *Chem. Commun.*, 2011, **47**, 496–498; (b) L. V. Meyer, J. Vogt, H. Schafer, M. Steinhart, R. Bottcher, A. Poppl, M. Mai, C. Feldmann and K. Müller-Buschbaum, *Inorg. Chem. Front.*, 2015, **2**, 237–245.
- 36 L. V. Meyer, F. Schönfeld, A. Zurawski, M. Mai, C. Feldmann and K. Müller-Buschbaum, *Dalton Trans.*, 2015, **44**, 4070–4079.
- 37 J. I. Steinfeld, J. S. Francisco and W. L. Hase, *Chemical Kinetics and Dynamics*, Prentice Hall, 2nd edn, 1998.
- 38 J. U. Wieneke and C. Staudt, *Polym. Degrad. Stab.*, 2010, **95**, 684–693.
- 39 R. H. B. Bouma, A. Checchetti, G. Chidichimo and E. Drioli, *J. Membr. Sci.*, 1997, **128**, 141–149.
- 40 BASF Ultrason S 6060 ISO Data Sheet.
- 41 A. Zurawski, J. C. Rybak, L. V. Meyer, P. R. Matthes, V. Stepanenko, N. Dannenbauer, F. Würthner and K. Müller-Buschbaum, *Dalton Trans.*, 2012, **41**, 4067–4078.